Powder Technology 272 (2015) 142–152

Contents lists available at ScienceDirect

Powder Technology

journal homepage: www.elsevier.com/locate/powtec

CFD-PBM modeling polydisperse polymerization FBRs with simultaneous particle growth and aggregation: The effect of the method of moments

Ya Yao [a], Jun-Wei Su [b], Zheng-Hong Luo [a,*]

[a] Department of Chemical Engineering, School of Chemistry and Chemical Engineering, Shanghai Jiao Tong University, Shanghai 200240, PR China
[b] School of Human Settlements and Civil Engineering, Xi'an Jiaotong University, Xi'an 710049, PR China

ARTICLE INFO

Article history:
Received 26 July 2014
Received in revised form 7 September 2014
Accepted 20 November 2014
Available online 6 December 2014

Keywords:
Polydisperse polymerization FBRs
CFD-PBM
Method of moments
Hydrodynamics

ABSTRACT

Real solid systems in polymerization fluidized bed reactors (FBRs) are characterized by wide particle size distributions that change continuously due to particle micro-behavior, growth and aggregation, etc. Simulations of such gas–solid flow hydrodynamics require the solution of a coupled computational fluid dynamics (CFD)-population balance equation (PBE) model, i.e. the CFD-PBM. Therefore, the analysis of the existing numerical methods for solving the PBE is important for the ability of the numerical prediction of the coupled model. Three representatively numerical moment-based methods, namely the quadrature method of moments (QMOM), the direct quadrature method of moments (DQMOM) and the fixed pivot quadrature method of moments (FPQMOM), were used to solve the PBE for evaluating the effect of numerical method. Comparative results demonstrated the suitability of the FPQMOM for modeling polymerization FBRs with simultaneous polymerization particle growth and aggregation.

1. Introduction

In general, the real heterogeneous polymerization systems in fluidized bed reactors (FBRs) are polydisperse [1–3]. FBR is also one of the most widespread commercial reactors to produce polyolefin due to its simple construction and excellent transfer capabilities [4]. In such systems, the particle growth (due to polymerization kinetics) and particle aggregation (due to particle softening at high temperature) can enlarge the polydispersity [5]. In an effort to consider the effect of the polydispersity of particles on the flow behaviors, a coupled model, namely CFD-PBM, must be employed [6]. Recently, there are papers on the kinetic theory application in polydispersed cases (i.e. the CFD-PBM), which are also on verification and validation study of some polydisperse kinetic theories. However, the current work is on the solution of PBM.

Since the existence and uniqueness of the solution of population balance equation (PBE) is a standard subject in mathematical textbooks [6], the PBE can be solved at least in principle. Unfortunately, there are few analytical solution strategies, while these available strategies are only for simplified problems thus cannot be adopted for real systems [7]. Numerical methods, as the primary solution strategies, can be classified into the method of classes [8], the Monte Carlo method [9] and the method of moments (MOMs) [10]. Among them, the MOMs are preferable to coupling the PBE solution with CFD codes for polydisperse multiphase flow simulations due to their easy application, reasonable accuracy and moderate computational cost [11–18]. The MOMs tracks a selected set of lower order moments of the particle distribution function. However, the MOMs suffer from the "closure problem" [10], which limits its usage in the academic community at early stage.

In order to solve this closure problem, McGraw introduced Gaussian quadrature approximation to the particle size distribution (PSD) [12], and since then, some new improved MOMs, such as the QMOM [12–15], the DQMOM [19–21] and the sectional quadrature method of moments (SQMOM) [22], were suggested. Regarding their detailed descriptions, the readers are referred to works [12–15,19–27]. The QMOM and the DQMOM are the most promising moment methods at present. However, one has to resort to the product-difference (PD) algorithm to calculate the quadrature abscissas and weights with them (QMOM at each time step and DQMOM at start). The actual values for abscissas and weights are not restricted to be positive in PD algorithm itself, which leads to the appearing of the zero abscissas if the number of the moments tracked is high (10 for instance). Thus, their application in tracking large number of moments is limited [27]. Moreover, they would become computationally intractable, and in the worst case numerical instability could occur [28]. Recently, Gu et al. proposed a new MOM based on the fixed pivot moments, namely the fixed pivot quadrature method of moments (FPQMOM), to solve the above problems for PBEs [29]. Different from the QMOM and the DQMOM, the most important feature of the FPQMOM is that constant characteristic abscissas are artificially specified at the beginning of the simulation and remain the same throughout the whole simulation. Also an efficient and accurate algorithm is used to solve the Vandermonde linear system

* Corresponding author. Tel./fax: +86 21 54745602.
E-mail address: Luozh@sjtu.edu.cn (Z.-H. Luo).

http://dx.doi.org/10.1016/j.powtec.2014.11.037
0032-5910/

to obtain the weights of Dirac Delta function, which is different from the PD algorithm as described earlier in the QMOM and the DQMOM. Nevertheless, the FPQMOM has not been used to solve the PBEs within the CFD-PBM model since it was suggested by Gu et al. in 2009 [29–32]. They only presented the basic steps for coupling the FPQMOM with CFD for modeling multiphase flows.

Considerable attention has been devoted in recent years to the application of these MOMs except the FPQMOM to solve PBEs in gas–solid FBRs [33–43]. Comparative analysis of MOMs in FBRs has also been reported [42]. For instance, Ahmadzadeh et al. described the evolution and growth of the particle size in gas–solid rotating fluidized bed olefin polymerization reactors using a CFD-PBM. The standard method of moments and QMOM were used to solve the PBEs [33]. Mazzei et al. described the behaviors of polydisperse fluidized multiphase systems in a Eulerian framework incorporating the PBEs. In their work, a novel version of the QMOM was formulated and implemented [34]. Luo et al. simulated the gas–solid flows in polymerization FBRs using a CFD-PBM [35,36], and later extended the CFD-PBM to simulate the gas–solid flows in multizone circulating polymerization reactors [37]. The QMOM was adopted for solving the PBEs in these works. Recently, Li et al. used the QMOM to solve the PBM for realizing the combination of the CFD model and PBM for simulating FCC risers [38]. In addition, the DOMOM has been used by Fan et al. [21], Fan and Fox [39] and Mazzei et al. [40] to simulate gas–solid flows in dense fluidized beds. Dutta et al. simulated the hydrodynamic behavior of dispersed gas–solid flow in an industrial-scale FCC riser using a CFD-PBM and the DQMOM was used to solve the PBEs [41]. Mazzei comparatively analyzed the QMOM and DQMOM transport equations obtained to describe the gas–solid fluidization dynamics of two inert polydisperse powders initially segregated, showing their limitations for modeling inhomogeneous polydisperse fluidized powders [42]. However, in these works [33–42], the reactions within polydisperse solid particles were generally ignored and the examination in a CFD-PBM was performed at cold model condition without particle growth due to reaction kinetics. In addition, although the FPQMOM is excellent in principle, there is still absence of examination and comparative analysis in gas–solid FBRs for it. To the best of our knowledge, there is so far no open literature on assessment of different MOMs in simulating gas–solid flows in polydisperse polymerization FBRs [43]. Thus, the quantitative understanding of the effect of MOM type on the gas–solid flow behavior remains unclear, which needs further investigation.

In this work, a two-dimensional (2D) CFD-PBM coupled modeling approach is proposed to investigate the gas–solid hydrodynamics in a polydisperse propylene polymerization FBR. In the coupled model, the Eulerian–Eulerian two-fluid model involving the kinetic theory of granular flow, the population balance and the heat exchange equations. Three representative MOMs, i.e. QMOM, DQMOM and FPQMOM, are used to solve the PBEs in the coupled model to investigate their effects on the bed hydrodynamics. Some of the results are also validated with classical calculation.

2. Mathematical model and numerical simulations

2.1. Simulated reactor

To obtain the effect of the MOMs on the gas–solid hydrodynamics in a polydisperse polymerization FBR, an experiment-scale FBR was studied as in our previous works [44]. Fig. 1 illustrates the FBR configuration and the CFD grid.

2.2. The CFD-PBM and the MOMs

The 2D CFD-PBM model in this work is analogous to that reported in our previous works [35,36,44] with minor difference. The most significant difference is the MOM used in the CFD-PBM. Besides the QMOM, the DQMOM and the FPQMOM are applied herein. For a detailed description of the 2D CFD-PBM, the readers are encouraged to refer to our previous work [35,36,44]. Due to space limitation, two phase dynamics equations are listed in Table 1. Herein, we only describe PBEs and MOMs.

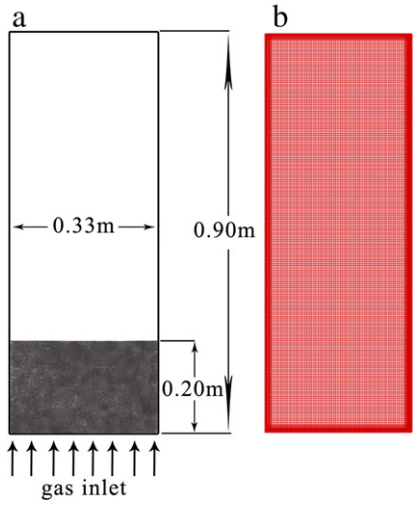

Fig. 1. (a) Reactor configuration and (b) CFD grid.

2.2.1. The PBEs

The general form of the univariate PBE is:

$$\frac{\partial n(L;t)}{\partial t}+\nabla\cdot\left[\vec{u}\,n(L;t)\right]=-\frac{\partial}{\partial L}[G(L)n(L;t)]+B_{ag}(L;t)-D_{ag}(L;t)+B_{br}(L;t)-D_{br}(L;t) \tag{1}$$

The moments of the PSD first introduced by Hulburt and Katz are defined as [10]:

$$m_k(t)=\int_0^\infty n(L;t)L^k dL \qquad k=0,1,\cdots,N-1 \tag{2}$$

In addition, the Sauter Diameter (d_{32}) is used as the mean particle diameter given by

$$d_{32}=\frac{m_3}{m_2} \tag{3}$$

Substituting Eq. (2) into Eq. (1) yields:

$$\frac{\partial m_k}{\partial t}+\nabla\cdot\left(\vec{u}\,m_k\right)=-\int_0^\infty kL^{k-1}G(L)n(L;t)dL+\overline{B}_{ag}(t)-\overline{D}_{ag}(t)+\overline{B}_{br}(t)-\overline{D}_{br}(t) \tag{4}$$

2.2.2. Three different moment methods

2.2.2.1. The QMOM. The QMOM uses a Gaussian quadrature approximation expressed as follows [12–15]

$$m_k=\int_0^\infty n(L;t)L^k dL\approx\sum_{i=1}^{N}w_iL_i^k \tag{5}$$

where, w_i and L_i are obtained with PD algorithm from the first 2 N moments [48].

Table 1
The CFD model.

Description	Equation
Eulerian–Eulerian Two Fluid Model	
Continuity equation for phase q	$\frac{\partial}{\partial t}\left(a_q\rho_q\right)+\nabla\cdot\left(a_q\rho_q\overrightarrow{v_q}\right)=\dot{m}_{sp}$
Momentum balance equation for gas	$\frac{\partial}{\partial t}\left(a_g\rho_g\overrightarrow{v}_g\right)+\nabla\cdot\left(a_g\rho_g\overrightarrow{v}_g\cdot\overrightarrow{v}_g\right)=-a_g\nabla p+\nabla\cdot\overline{\overline{\tau}_g}+\beta\left(\overrightarrow{v}_s-\overrightarrow{v}_g\right)+a_g\rho_g g$
Momentum balance equation for solid	$\frac{\partial}{\partial t}\left(\alpha_s\rho_s\overrightarrow{v}_s\right)+\nabla\cdot\left(\alpha_s\rho_s\overrightarrow{v}_s\overrightarrow{v}_s\right)=-\alpha_s\nabla p-\nabla p_s+\nabla\cdot\overline{\overline{\tau}_s}+\beta\left(\overrightarrow{v}_g-\overrightarrow{v}_s\right)+\alpha_s\rho_s g$
Energy balance equation for gas	$\frac{\partial}{\partial t}\left(\alpha_g\rho_g h_g\right)+\nabla\cdot\left(\alpha_g\rho_g v_g h_g\right)=-\alpha_g\frac{\partial p_g}{\partial t}+\overline{\overline{\tau}}_g:\nabla v_g-\nabla\cdot q_g+\sum_{p=1}^{n}\left(Q_{gs}+\dot{m}_{gs}h_{gs}-\dot{m}_{sg}h_{sg}\right)$
Energy balance equation for solid	$\frac{\partial}{\partial t}\left(\alpha_s\rho_s h_s\right)+\nabla\cdot\left(\alpha_s\rho_s v_s h_s\right)=-\alpha_s\frac{\partial p_s}{\partial t}+\overline{\overline{\tau}}_s:\nabla v_s-\nabla\cdot q_s+\sum_{p=1}^{n}\left(Q_{sg}+\dot{m}_{sg}h_{sg}-\dot{m}_{gs}h_{gs}\right)+\Delta Q_{rs\alpha}$
Heat exchange model	$Q_{gs}=\kappa_{gs}(T_s-T_g)$
	$\kappa_{gs}=\frac{6\kappa_g\alpha_g\alpha_s Nu_s}{d_s^2}$
Gunn formula [45]	$Nu_s=\left(7-10a_g+5a_g^2\right)\left(1+0.7\mathrm{Re}_s^{0.2}\ ,\mathrm{Pr}^{1/3}\right)+$
	$\left(1.33-2.4a_g+1.2a_g^2\right)\mathrm{Re}_s^{0.7}\ ,\mathrm{Pr}^{1/3}$
EMMS drag model [46,47]	$\begin{cases}\beta_{EMMS}=\frac{3}{4}\frac{\alpha_s\alpha_g\rho_g\left\lvert\overrightarrow{v_s}-\overrightarrow{v_g}\right\rvert}{d_s}C_D\omega\alpha_g\geq 0.74\\ \beta_{\mathrm{Ergun}}=150\frac{\alpha_s{}^2\mu_g}{\alpha_g d_s^2}+1.75\frac{\alpha_s\rho_g\left\lvert\overrightarrow{v_s}-\overrightarrow{v_g}\right\rvert}{d_s}\quad \alpha_g<0.74\end{cases}$
	$\omega=\begin{cases}-0.5760+\frac{0.0214}{4\left(a_g-0.7463\right)^2+0.0044} & 0.74\leq a_g\leq 0.82\\ -0.0101+\frac{0.0038}{4\left(a_g-0.7789\right)^2+0.0040} & 0.82<a_g\leq 0.97\\ -31.8295+32.8295a_g & a_g>0.97\end{cases}$
	$C_D=\begin{cases}\frac{24}{\alpha_g\mathrm{Re}_s}\left[1+0.15\left(\alpha_g\mathrm{Re}_s\right)^{0.687}\right] & \mathrm{Re}_s\leq 1000\\ 0.44 & \mathrm{Re}_s>1000\end{cases}$
Gas phase stress tensor	$\overline{\overline{\tau}}_g=\alpha_g\mu_g\left(\nabla\overrightarrow{v}_g+\nabla\overrightarrow{v}_g{}^T\right)$
Solid phase stress tensor	$\overline{\overline{\tau}}_s=\alpha_s\mu_s\left(\nabla\overrightarrow{v}_s+\nabla\overrightarrow{v}_s{}^T\right)+\alpha_s\left(\lambda_s-\frac{2}{3}\mu_s\right)\nabla\cdot\overrightarrow{v}_s\bar{\bar{I}}$
Kinetic Theory of Granular Flow (KTGF) [56]	
Complete granular temperature [57,58]	$\Theta_s=\frac{1}{3}\overrightarrow{v_s'}\overrightarrow{v_s'}$
	$\frac{3}{2}\left[\frac{\partial}{\partial t}\left(\rho_s a_s\Theta_s\right)+\nabla\cdot\left(\rho_s a_s\overrightarrow{v_s}\Theta_s\right)\right]=\left(-p_s\bar{\bar{I}}+\overline{\overline{\tau}}_s\right):\nabla\overrightarrow{v_s}$
	$+\nabla\cdot\left(k_{\Theta_s}\nabla\Theta_s\right)-\gamma_{\Theta_s}+\phi_{gs}$
	$k_{\Theta_s}=\frac{15\rho_s d_s a_s\sqrt{\pi\Theta_s}}{4(41-33\eta)}\left[1+\frac{12}{5}\eta^2(4\eta-3)a_s g_0+\frac{16}{15\pi}(41-33\eta)\eta a_s g_0\right]$
	$\gamma_{\Theta_s}=\frac{12\left(1-e_s^2\right)g_0}{d_s\sqrt{\pi}}\rho_s a_s^2\Theta_s^{1.5}$
	$\phi_{\mathrm{gs}}=-3K_{gs}\Theta_s$
Algebraic equation of granular temperature	$0=\left(-p_s\bar{\bar{I}}+\overline{\overline{\tau}}_s\right):\nabla\overrightarrow{v}_s-\gamma_{\Theta_s}-3K_{gs}\Theta_s$
Radial distribution function	$g_o=\frac{1}{1-\left(a_s/a_{s,\max}\right)^{1/3}}$
Solid pressure	$p_s=a_s\rho_s\Theta_s[1+2g_o a_s(1+e_s)]$
Bulk viscosity	$\lambda_s=\frac{4}{3}a_s\rho_s d_s g_o(1+e_s)\sqrt{\frac{\Theta_s}{\pi}}$
Solids viscosity [59,60]	$\mu_s=\mu_{s,col}+\mu_{s,kin}+\mu_{s,fr}$
	$\mu_{s,col}=\frac{4}{5}a_s\rho_s d_s g_0(1+e_s)\sqrt{\frac{\Theta_s}{\pi}}$
	$\mu_{s,kin}=\frac{10d_s\rho_s\sqrt{\Theta_s\pi}}{96a_s(1+e_s)g_0}\left[1+\frac{4}{5}(1+e_s)a_s g_0\right]^2$
	$\mu_{s,fr}=\frac{p_s\cdot\sin\theta}{2\sqrt{I_{2D}}}$
Turbulent model [61,62]	
Standard $k-\varepsilon$ model	$\nabla\cdot\left(\rho_m k\overrightarrow{v_m}\right)=\nabla\cdot\left(\frac{\mu_{t,m}}{\sigma_\varepsilon}\nabla k\right)+G_{k,m}-\rho_m\varepsilon$
	$\nabla\cdot\left(\rho_m\varepsilon\overrightarrow{v_m}\right)=\nabla\cdot\left(\frac{\mu_{t,m}}{\sigma_\varepsilon}\nabla\varepsilon\right)+\frac{\varepsilon}{k}+\left(C_{1\varepsilon}G_{k,m}-C_{2\varepsilon}\rho_m\varepsilon\right)$
	$\rho_m=\sum_{i=1}^{N}a_i\rho_i$
	$\overrightarrow{v_m}=\frac{\sum_{i=1}^{N}a_i\rho_i\overrightarrow{v_m}}{\sum_{i=1}^{N}a_i\rho_i}$
	$\mu_{t,m}=\rho_m C_\mu\frac{k^2}{\varepsilon}$

By introducing the quadrature approximation, integrals of the density function are turned into summations, and Eq. (4) can be written as:

$$\frac{\partial m_k}{\partial t}+\nabla\cdot\left(\overrightarrow{u}m_k\right)=k\sum_{i=1}^{N}L_i^{k-1}G(L_i)w_i+\frac{1}{2}\sum_{i=1}^{N}w_i\sum_{j=1}^{N}w_j\left(L_i^3+L_j^3\right)^{k/3}\beta_{i,j}-\sum_{i=1}^{N}L_i^k w_i\sum_{j=1}^{N}w_j\beta_{i,j}+\sum_{i=1}^{N}w_i a_i\overline{b_i}-\sum_{i=1}^{N}L_i^k w_i a_i \quad (6)$$

where, $\beta_{i,j}=\beta(L_i,L_j)$, $a_i=a(L_i)$, $\overline{b_i}=\int_0^\infty L^k b(L|L_i)dL$ are aggregation kernel, breakage kernel and daughter distribution function, respectively.

2.2.2.2. The DQMOM. The DQMOM introduces the Gaussian approximation before moment transformation, and as a result, w_i and ζ_i ($\zeta_i=L_i w_i$) are tracked directly and the PD algorithm is no longer needed

during the simulation. The transport equations for them are written as [19–21]

$$\frac{\partial \omega_i}{\partial t} + \nabla \cdot \left(\vec{u} \cdot \omega_i\right) = a_i \tag{7}$$

$$\frac{\partial \zeta_i}{\partial t} + \nabla \cdot \left(\vec{u} \cdot \zeta_i\right) = b_i \tag{8}$$

where, a_i and b_i are evaluated via solving a linear system given by

$$A\alpha = d \tag{9}$$

where, the coefficient $A = [A_1\ A_2]$ is a $2\ N \times 2\ N$ matrix defined by:

$$A_1 = \begin{bmatrix} 1 & \cdots & 1 \\ 0 & \cdots & 0 \\ -L_1^2 & \cdots & -L_N^2 \\ \vdots & \vdots & \vdots \\ 2(1-N)L_1^{2N-1} & \cdots & 2(1-N)L_N^{2N-1} \end{bmatrix} \tag{10}$$

$$A_2 = \begin{bmatrix} 0 & \cdots & 0 \\ 1 & \cdots & 1 \\ 2L_1 & \cdots & 2L_N \\ \vdots & \vdots & \vdots \\ (2N-1)L_1^{2N-2} & \cdots & (2N-1)L_N^{2N-2} \end{bmatrix} \tag{11}$$

$$\alpha = [a_1 \cdots a_N, b_1 \cdots b_N]^T = \begin{bmatrix} a \\ b \end{bmatrix} \tag{12}$$

$$d = \begin{bmatrix} \overline{S}_0^{(N)} & \cdots & \overline{S}_{2N-1}^{(N)} \end{bmatrix}^T \tag{13}$$

where, the source term for the kth moment $\overline{S}_{2N-1}^{(N)}$ is written as:

$$\overline{S}_k^{(N)} = \int_0^\infty L^k S(L;t)dL \tag{14}$$

In addition, the source terms in Eq. (14) are the same as those in QMOM written as

$$\begin{aligned} \overline{S}_k^{(N)} = {} & k\sum_{i=1}^{N} L_i^{k-1} G(L_i) w_i + \frac{1}{2}\sum_{i=1}^{N} w_i \sum_{j=1}^{N} w_j \left(L_i^3 + L_j^3\right)^{k/3} \beta_{i,j} \\ & - \sum_{i=1}^{N} L_i^k w_i \sum_{j=1}^{N} w_j \beta_{i,j} + \sum_{i=1}^{N} w_i a_i \overline{b}_i - \sum_{i=1}^{N} L_i^k w_i a_i \end{aligned} \tag{15}$$

2.2.2.3. The FPQMOM. The fixed pivot quadrature method of moments (FPQMOM) adopts the following approximation of particle size distribution [29]:

$$n(V;t) = \sum_{i=1}^{N} \omega_i(t)\delta(V - V_i) \tag{16}$$

where, V_i is specified to be the N order Laguerre–Gaussian abscissas and remains constant throughout the simulation. It should be pointed out that the assumption in Eqs. (16) is different from that in QMOM in essence, although they look similar in form.

Based on the assumption in Eq. (16), the kth moment can be expressed as:

$$m_k(t) = \sum_{i=1}^{N} \omega_i(t) V_i^k \tag{17}$$

Eq. (17) can be written in matrix form as:

$$\begin{bmatrix} 1 & 1 & \cdots & 1 \\ V_1 & V_2 & \cdots & V_N \\ \vdots & \vdots & \ddots & \vdots \\ V_1^{N-1} & V_2^{N-1} & \cdots & V_N^{N-1} \end{bmatrix} \begin{bmatrix} \omega_1(t) \\ \omega_2(t) \\ \vdots \\ \omega_N(t) \end{bmatrix} = \begin{bmatrix} m_0(t) \\ m_1(t) \\ \vdots \\ m_{N-1}(t) \end{bmatrix} \tag{18}$$

Eq. (18) is the Vandermonde equation set. However, it's clear that the coefficient matrix is severely morbidity and this would result in poor accuracy if one solves it directly. Due to this, a special algorithm is adopted for the solving of Eq. (18) to obtain the weights (w_i) [49].

The transport equation for the kth moment is:

$$\begin{aligned} \frac{\partial m_k}{\partial t} + \nabla \cdot \left(\vec{u} m_k\right) = {} & k\sum_{i=1}^{N} V_i^{k-1} G(V_i) w_i + \frac{1}{2}\sum_{i=1}^{N} w_i \sum_{j=1}^{N} w_j \left(V_i + V_j\right)^k \beta_{i,j} \\ & - \sum_{i=1}^{N} V_i^k w_i \sum_{j=1}^{N} w_j \beta_{i,j} + \sum_{i=1}^{N} w_i a_i \overline{b}_i - \sum_{i=1}^{N} V_i^k w_i a_i \end{aligned} \tag{19}$$

2.2.3. Micro-behaviors kernels

2.2.3.1. The particle growth rate. $G(L_i)$ is related to the polymerization reaction rate and can be expressed as follows:

$$G(L_i) = \frac{d(L_i)}{dt} = \frac{R_p L_0^3}{3\rho_s L_i^2} \tag{20}$$

where, R_p is the polymerization reaction rate defined by Zacca et al.'s equation [50].

$$R_p = k_{p0} \exp\left(-\frac{E}{R(273.15 + t)}\right)[M]\left[C^*\right] \tag{21}$$

2.2.3.2. The aggregation kernel. Arastoorpour et al.'s model [51] with some modifications is adopted as the aggregation kernel in this work.

$$\beta_{i,j} = KK\left(L_i + L_j\right)^2 \sqrt{\frac{1}{L_i^3} + \frac{1}{L_j^3}} \tag{22}$$

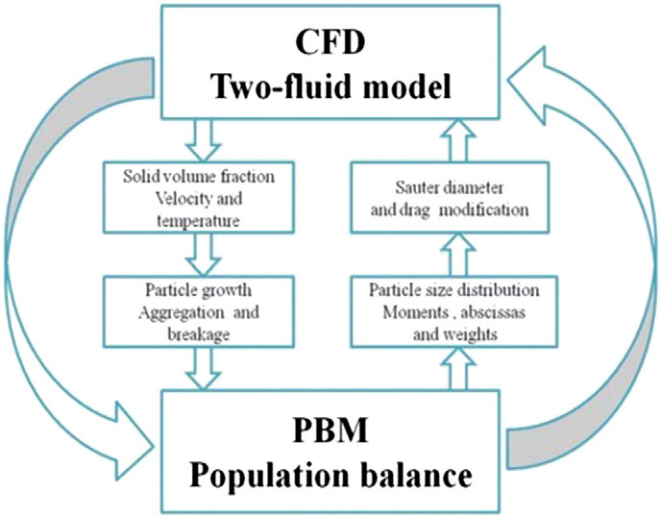

Fig. 2. The CFD-PBM coupled model.

Table 2
Main reaction parameters.

Parameter	Values
Solid	
Density, ρ_s	910 (kg m^{-3})
Heat capacity, $C_{p,s}$	2104 (J kg^{-1} K^{-1})
Thermal conductivity, $_s$	0.1584506 (W m^{-1} K^{-1})
Diameter, d_s	Sauter (m)
Gas	
Density, ρ_g	21.56 (kg m^{-3})
Heat capacity, $C_{p,g}$	1817 (J kg^{-1} K^{-1})
Thermal conductivity, $_g$	0.02306446 (W m^{-1} K^{-1})
Viscosity, μ_g	1.081×10^{-5} (Pa s)
composition	C_3H_6:Air = 6:1 (V:V)
Kinetic parameter	
Activation energy, E	5.04×10^4 (J mol^{-1})
Chemical heat release, ΔH	100 KJ mol^{-1}
Pre-exponential factor, k_{p0}	1.2×10^4 (m^3 mol^{-1} s^{-1})

The dimensionless coefficient *KK* is a function of particle temperature [52]

$$KK = kk_1 \exp\left(kk_2 T_s / T_{sf}\right) \tag{23}$$

where, $kk_1 = 4.0 \times 10^{-10}$,$kk_2 = 3.85$.

2.2.4. The CFD-PBM

In order to describe the evolution of the particle size distribution and its effects on the two-phase dynamics behaviors in polymerization reaction, we have to resort to PBEs. As a result, a CFD-PBM coupled model must be used. Fig. 2 is the schematic representation of CFD-PBM coupled model used in this work. In each time step, the solid volume fraction, particle velocity and temperature obtained by solving mass conservation, momentum conservation and energy conservation equations are used to calculate the particle growth and aggregation kernels in PBEs. Then the PBEs can be solved, and the Sauter Diameter is obtained to further modify the interphase force in CFD and enter the next time step. Thus, the CFD-PBM coupled model is built.

2.3. Simulation conditions and modeling method

As mentioned above, the 2D CFD-PBM model is analogous to that reported in our previous works [35,36,44], thus, most of the model parameters are obtained from those literatures directly and listed in Tables 2 and 3. The initial PSD with mean particle size of 1.835628×10^{-4} m is shown in Fig. 3. The initial moments can be calculated using the following formula:

$$m_k \approx \sum\left(n(L) \cdot L^k \cdot \Delta L\right) \tag{24}$$

Table 3
Main model parameters.

Description	Value
Granular viscosity	Gidaspow et al. [59]
Granular bulk viscosity	Lun et al. [56]
Frictional viscosity	Schaeffer et al. [60]
Angle of internal friction	30°
Granular temperature	Algebraic
Inlet boundary condition	Velocity inlet
Outlet boundary condition	Pressure outlet
Wall boundary condition	No slip for air, free slip for solid phase, the adiabatic heat-transfer equation
Initial bed height	0.2 m
Initial volume fraction of solid phase	0.63
Operating pressure	1.40×10^6 Pa
Inlet gas velocity	0.3 m · s^{-1}
Inlet gas temperature	313 K
Restitution coefficient	0.9
Turbulent kinetic energy	0.00036 m^2/s^2
Turbulent dissipation rate	8.2×10^{-5} m^2/s^3
Maximum iterations	50
Convergence criteria	1×10^{-3}
Time step	1×10^{-3} s

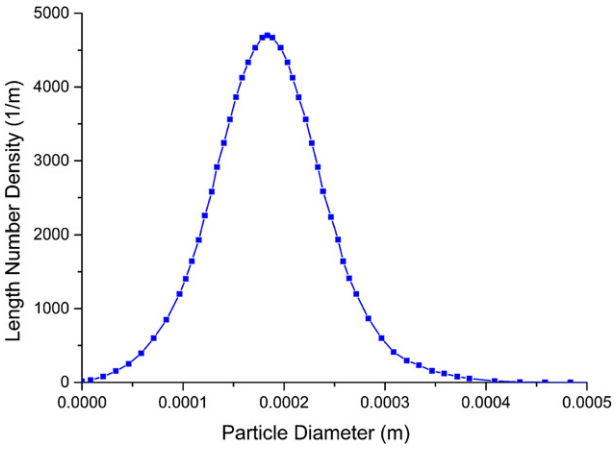

Fig. 3. The initial PSD profile.

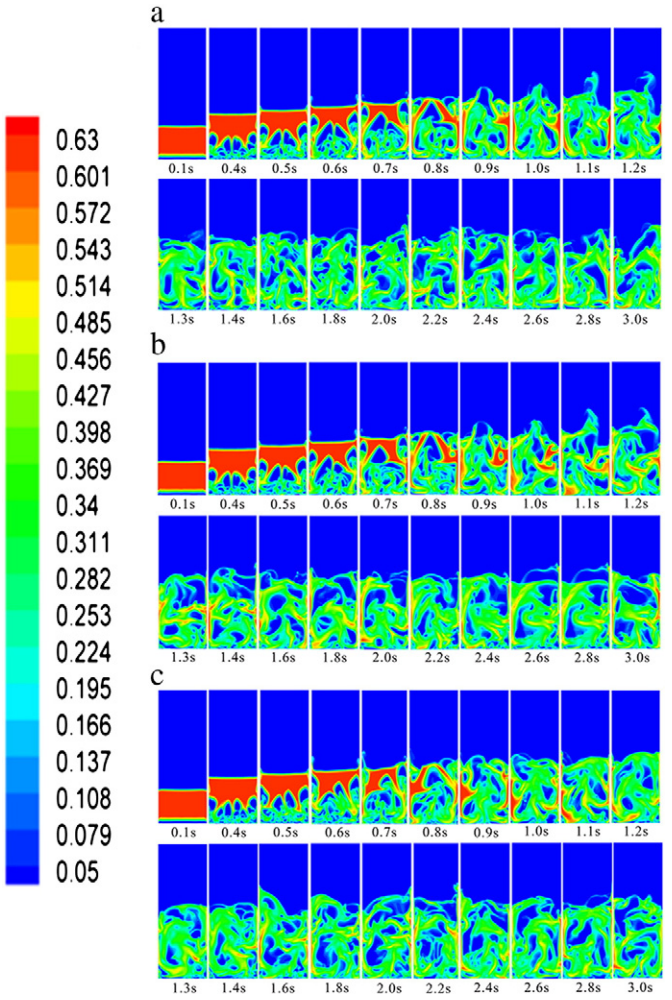

Fig. 4. The fluidization process from 0.1 s to 3.0 s using (a) QMOM, (b) DQMOM, and (c) FPQMOM.

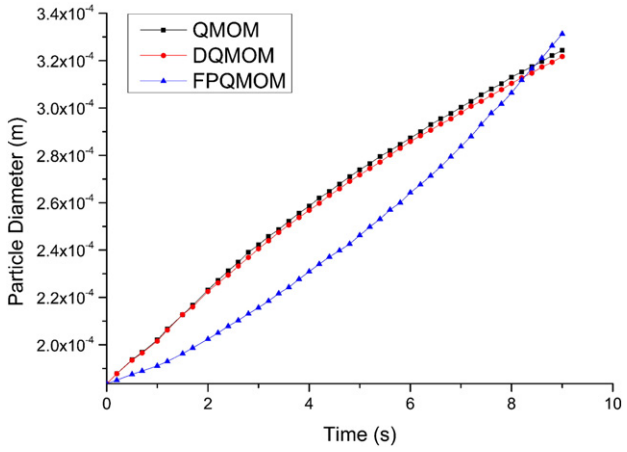

Fig. 5. The evolution of Sauter diameter versus time.

Based on Refs. [13] and [21], $N = 3$ with the QMOM and the DQMOM offers the best tradeoff between accuracy and computational cost. In addition, the FPQMOM was implemented with 6 nodes. Six order Laguerre–Gaussian abscissas have the values of {0.22284659, 1.1889321, 2.9927363, 5.7751436, 9.8374323, 15.982909}. However, based on the nature of our system, we used the values of {0.000022284659, 0.00011889321, 0.00029927363, 0.00057751436, 0.00098374323, 0.0015982909} as the characteristic volumes with the FPQMOM.

The 2D CFD-PBM simulations were performed within the commercial CFD package FLUENT 6.3.26 (Ansys Inc., US) with double precision mode. The discretization scheme used in 0–2 s is the first-order upwind to increase the stability of the solution procedure. And the second-order upwind discretization scheme is used in 2–10 s to get more accurate numerical results. The phase coupled SIMPLE algorithm was used to decouple pressure and velocity [53]. The EMMS drag model [46,47], DQMOM, FPQMOM and source terms were defined via external user-defined scalars (UDS) and functions (UDF). The grid sensitivity was carried out previously, which indicated that a total amount of 15,520 cells was adequate to obtain realistic results in our FBR [44]. In addition, the simulations were performed in a platform of Intel Pentium G630 running on 2.7 GHz with 4 GB of RAM.

3. Results and discussion

Herein, in this section, the fluidization processes using three MOMs are investigated first to explain why we collect the time-averaged values from 2 to 10 s. Next, the evolutions of the particle diameter and the pressure drop using three MOMs are compared. Then, the effects of different MOMs on the flow characteristics and temperature distributions are studied. Finally, the computational efficiencies with three MOMs are discussed.

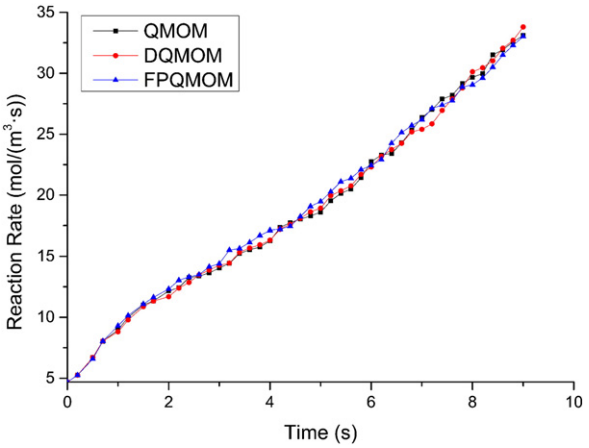

Fig. 6. The reaction rate as a function of time.

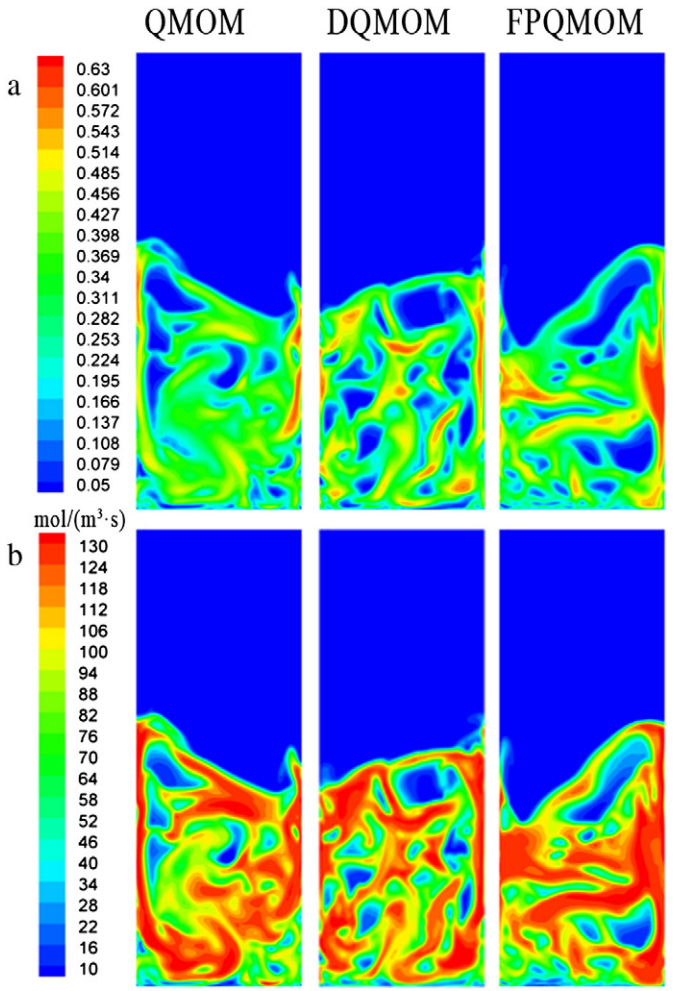

Fig. 7. (a) The volume fraction using three moment methods at 12 s. (b) The reaction rate using three MMs at 12 s.

3.1. The fluidization process

Fig. 4 demonstrates the relatively fast fluidization processes from 0.1 to 3 s using all three MOMs are similar. The whole bed begins to expand at 0.1 s. Next, the bubbles appear and move along the gas flow direction, which results in a uniform particle mixing in the FBR. The bed surface remains stable from 1.4 s, which means that the whole bed can be considered reaching a complete fluidization condition after 2 s. Therefore, the related variables (e.g. particle velocity, solid concentration) are assumed basically unchanged since 2 s. Based on this point, the time-averaged values used in the following sections are obtained from 2 to 10 s.

3.2. The evolution of mean particles size

Fig. 5 shows the evolution of Sauter Diameter as a function of polymerization time using the three MOMs. As shown in Fig. 5, using the QMOM and the DQMOM, a similar curve can be obtained, the slope of which (i.e. the rate of particles enlargement) decreases with polymerization proceeding. However, using the FPQMOM, the opposite trend can be predicted. Namely, using the FPQMOM, the increase rate of mean particle size is small at the initial stage of polymerization and then

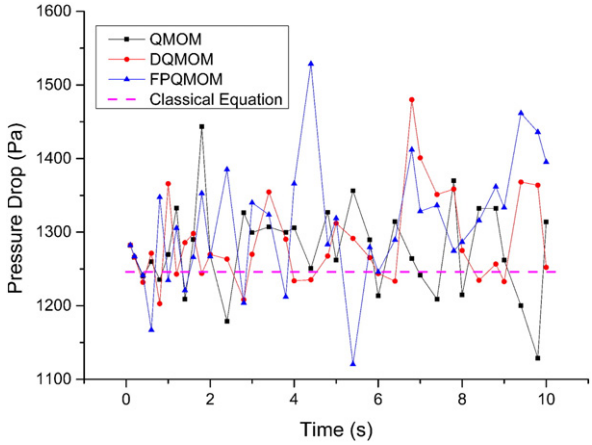

Fig. 8. The pressure drop as a function of flow time.

becomes faster. In the later stage the increase rate surpasses those predicted by the QMOM and the DQMOM. Arastoopour et al.'s experiment data shows that large size particles favored the agglomeration of particles [51]. In addition, Arastoopour et al. also demonstrated that the enlargement rate of particle size was proportional to particle diameter in polymerization reaction system [51]. Accordingly, the particle enlargement rate increases with the polymerization process. Furthermore, the olefin polymerization is a highly exothermic reaction, which leads to the increase of the bed temperature during the polymerization. Therefore, the reaction rate increases according to Eq. (21) (see Fig. 6). On the other hand, in the polymerization system, the particles easily break into many small pieces if the system temperature is low while agglomerate together to a bigger one at high temperature (when the temperature approaches to the melting point of polymers). The FBR is usually operated at a relatively high temperature to maintain reasonable polymerization rate and high catalytic activity in industry. In addition, the reaction rate is also related to the amount of particles (see Fig. 7). In short, the rate of particles enlargement is faster when the particle clusters size is bigger, which means that the FPQMOM can predict the most realistic evolution of particles size with the polymerization proceeding among the three MOMs.

3.3. The evolution of pressure drop

It is well known that the bed pressure drop is one of the most important parameter in the successful design and scale up of FBRs which can be calculated via the buoyant weight of the suspension expressed as follow [54].

$$\Delta P_s = \left(\rho_s - \rho_g\right)(1-\phi)gH \tag{25}$$

It's necessary to consider the effect of gas phase weight on the pressure drop because the gas phase density is up to 21.56 kg · m^{-3} in our work:

$$\Delta P_g = \phi\rho_g gH \tag{26}$$

Fig. 8 gives the comparison between the pressure drop obtained by both theoretical equation and our numerical simulation using three MOMs. The theoretical calculated value based on Eqs. (25) and (26) is 1246 Pa. It clearly shows that the simulated results can approximately meet the calculated value. Since the bed heights predicted by the three MOMs have little difference (see Fig. 4), the weights of suspension in bed are also similar. However, the simulated pressure drop values fluctuations due to the violent motions of particles in the actual bed. The FPQMOM can predict more severe fluctuation than the other two before 6 s. The reason is that FPQMOM can give the smaller particle size before 8 s, especially before 6 s (see Fig. 5). And the motions of smaller particles are more turbulent.

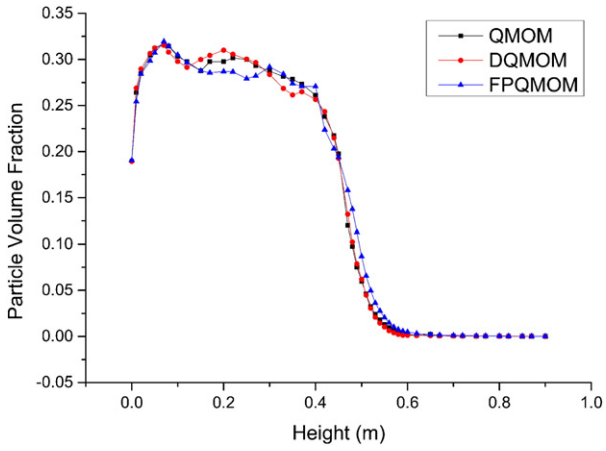

Fig. 9. Variation of time-averaged particle volume fraction along the bed (the data shown in this figure is the average of a plane).

3.4. The time-averaged particle volume fraction distribution

Fig. 9 illustrates the comparison of the predicted time-averaged particle volume fraction variation along the gas flow direction using the three MOMs, which clearly reveals that three curves have the similar changing trend. At the bottom of the FBR (0–0.1 m), the particle volume fraction is lower than that of the overall bed because of the effect of the inlet gas. With the increase of bed height within the dense phase (0.1–0.4 m), the particle concentration keeps stable due to the excellent mass transfer ability of the FBR, which results in a uniform particle mixing. Above 0.4 m, the particle concentration decreases sharply and the state of dilute phase reached. Then higher than 0.6 m, the particles are very few and their amount can be assumed to be zero. The overall trend is in qualitative agreement with the simulated results obtained by other researches [46,47,55]. Besides, Fig. 9 also shows that FPQMOM can predict the smaller particle volume fraction than the other two when the bed height is relatively low while obtain the bigger value when the height is high. This is due to the particle size calculated by FPQMOM is smaller before 8 s (see Fig. 5) and the smaller one can move to higher bed.

Fig. 10 shows the simulated time-averaged particle volume fraction profile in the radial direction at the heights of 0.2 m and 0.5 m using the three MOMs. The obvious existence of core-annular structure of the flow is predicted by all MOMs. The particle volume fraction is bigger near the wall due to the wall attachment effect. However, the particle concentration is lower than that of the bed at the wall. This is because the wall boundary condition for gas is set as no slip in this work. So it's more easily for gas to gather at the wall, which results in the smaller volume fraction of particle. Furthermore, the phenomenon that "FPQMOM can predict the smaller particle volume fraction than the other two when the bed height is relatively low while obtain the bigger one when the height is high" can be seen intuitive in Fig. 10.

In summary, all the MOMs can qualitative predict the realistic particle volume fraction distribution. However, due to the difference of the particle size calculated by FPQMOM, the solid volume fraction predicted by it is also distinctive.

3.5. The time-averaged vertical particle velocity distribution

The comparison of the simulated time-averaged vertical particle velocity distribution at heights of 0.2 m and 0.5 m using the three MOMs

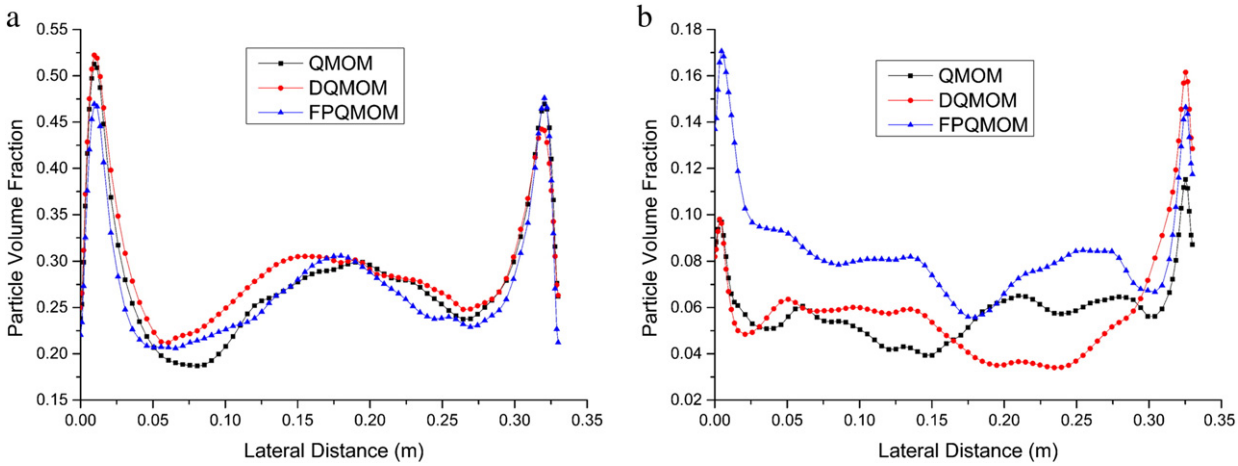

Fig. 10. Time-averaged particle volume fraction variation along the radial direction at (a) h = 0.2 m; and (b) h = 0.5 m.

are shown in Fig. 11. One can observe the clear existence of core-annular structure using the three MOMs (see Fig. 11(a)). One peak appears in the central region because the particles are entrained upwards by the gas. However, the particles fall down along the wall in the annular region. The overall changing trend of the curve is from the positive value in the center to the negative value near the wall. But a small decrease of the particles velocity can be observed at the wall. This is due to the fact "it's more easily for gas to gather at the wall", which we analyzed in Fig. 10. So the resistance force on particles applied by gas (drag force) is bigger. In addition, Fig. 11(b) reveals that all the velocity of particles is negative at the height of 0.5 m. That's to say all the particles are fall down under gravity effect at the higher plane. Meanwhile there appear two peaks in the figure. This can also well fit the simulated results in Refs. [55,63].

3.6. The particle temperature distribution

Temperature distribution is a key indicator for the efficiency of the operation in industrial FBRs. The reaction system will be forced to stop if some hot spots appear, and this will lead to great damage. Herein, the simulated gas and solid phase temperature variation along the axial direction using the three MOMs are shown in Fig. 12. From Fig. 12, the similar curves can be obtained using the three MOMs. Due to the feeding of the cool fresh gaseous monomers (313.15 K), the gas and particle temperature at the bottom of the FBR is lower. In the meanwhile, the gas temperature is lower than the solid temperature cause by the same reason. Then the temperatures show a significant rise with the bed height since the olefin polymerization is a highly exothermic reaction. Thanks for the excellent mass and heat transfer capability of the FBRs, the released heat can be removed promptly by gas. Hence the change of the temperature of gas and particle with height is little. But the increase trend is still clear. So the highest temperature along the axial direction appears at the top of the FBR.

Fig. 13 displays the predicted particle temperature profile in the plane at the heights of 0.2 m and 0.5 m. It can be seen from Fig. 13(a) that the particle temperature distribution is uneven at the lower section of the FBR due to the consideration of PSD and polymerization [35]. Furthermore, the temperature near the wall is higher than that at other position in the plane. This is due to that the particles are easily attached to the wall (see Fig. 10), so the reaction heat release is also greater there. However, according to Fig. 13(b), it's relatively less uneven of the solid temperature distribution at the higher plane. It's due to the fewer particles in the dilute phase, and corresponding, the heat can disperse to the whole section more easily. In addition, because the reaction heat release is related to the solid volume fraction. The temperature distribution is similar to the particle volume fraction distribution (compare Figs. 13 and 10), but also exist some difference. The difference is caused by the excellent heat remove capability of gas.

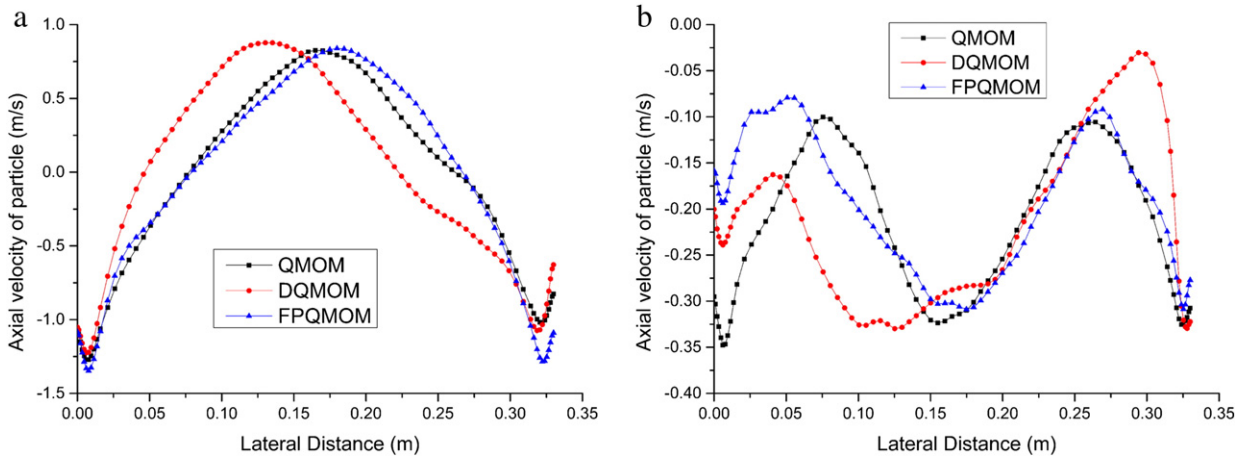

Fig. 11. Time-averaged vertical particle velocity variation along the radial direction at (a) h = 0.2 m; and (b) h = 0.5 m.

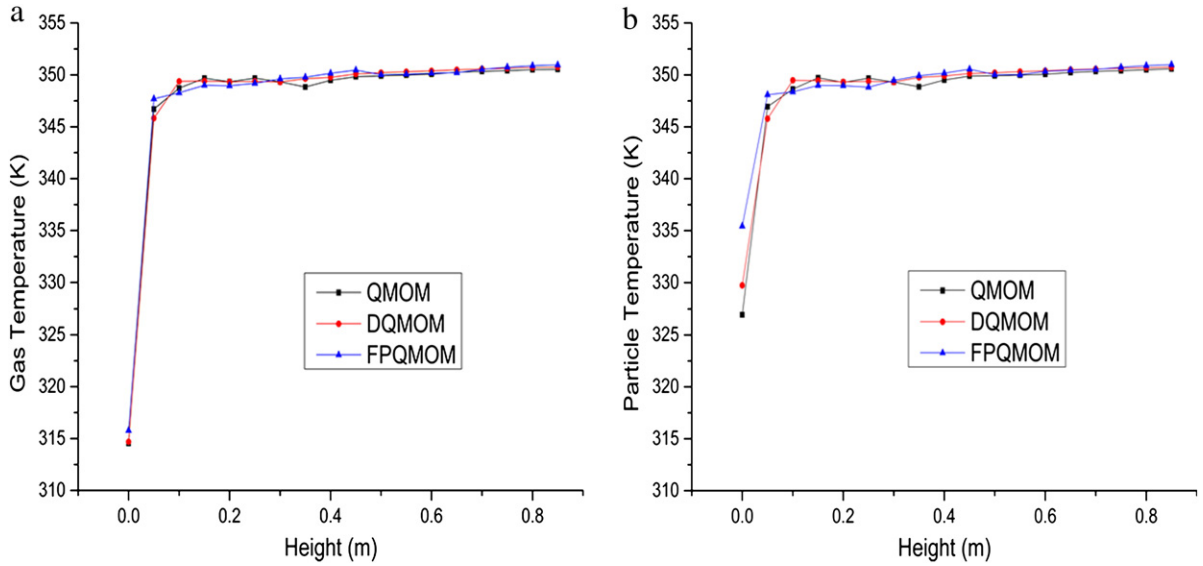

Fig. 12. The evolution of temperature of (a) gas; and (b) solid along the axial direction (at steady state and the data shown in this figure is the average of a plane).

Therefore, the solid temperature distribution also depends on the temperature of gas.

3.7. The computational time

The CPU time is an important factor to evaluate whether the MOM is effective [64]. By theoretical analysis for the three MOMs used in our work, six UDSs are added to represent six moments with three nodes QMOM. And the abscissas and weights can be back-calculated by resorting to the PD algorithm in every time step. But, due to the need of finding the values of a symmetric matrix in a PD algorithm, the real time consumption is relatively bigger. However, with three nodes DQMOM, six UDSs are also coupled to track three abscissas and three weights directly. Thus the PD algorithm can be avoided so that the real time cost is reduced. But the source term in DQMOM is more complex, which can increase the computation time. Using FPQMOM, there are also six UDSs added to track six moments. Because of the constant characteristic volumes, the efficient algorithm used to calculate weights, and the identical source terms with those in QMOM, the computational process with FPQMOM is the most efficient. Based on the above theoretical analysis, the sequence of the CPU time with three MOMs is: QMOM > DQMOM > FPQMOM. And the simulated results showed in Table 4 can also confirm our conclusion.

4. Conclusions

This work aims at choosing the most appropriate MOM for solving the PBEs in CFD-PBM model framework. Three representative methods, QMOM, DQMOM and FPQMOM are implemented in our coupled model for comparison. Numerical results of 2D FBR reveal: (1) the FPQMOM can predict that the rate of particles enlargement is faster where the particle clusters size is bigger, which is observed in experiment. However, the QMOM and the DQMOM yield the opposite variation trend. (2) All the three MOMs can obtain the reasonable pressure drop variation, time-averaged flow field and temperature distribution at steady. (3) The computational load of the FPQMOM is the smallest among the MOMs presented in this work.

Meanwhile, the FPQMOM and the DQMOM are superior to the QMOM in theory, because PD algorithm is avoided. However, in FPQMOM, constant positive characteristic abscissas are used, and the

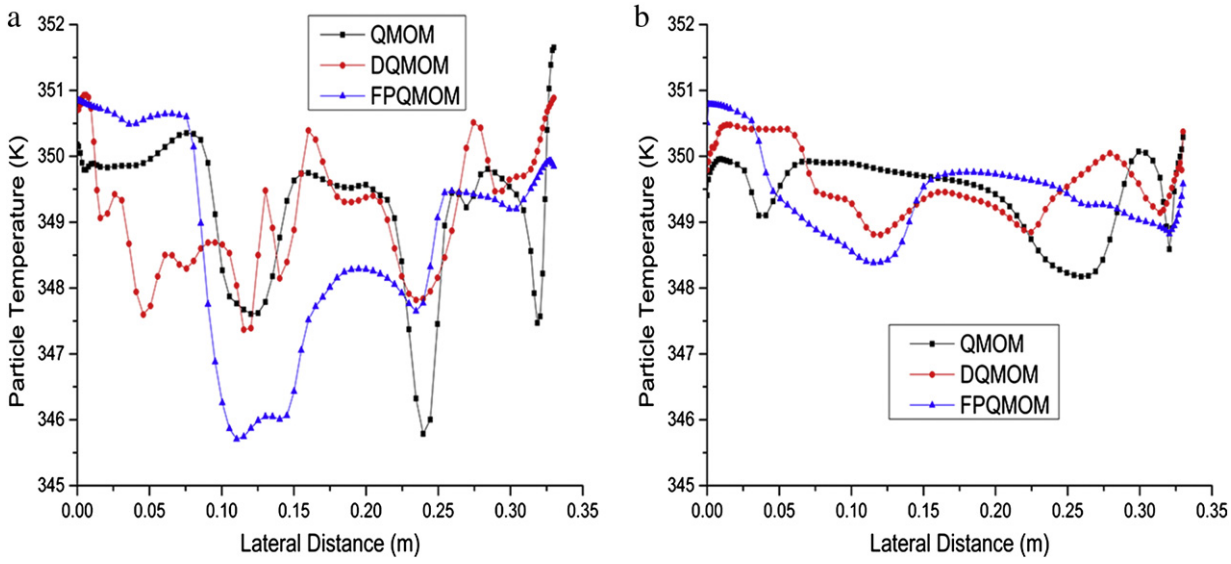

Fig. 13. Particle temperature variation along the radial direction at (a) h = 0.2 m; and (b) h = 0.5 m (at steady state).

Table 4
The computation time.

	QMOM	DQMOM	FPQMOM
CPU time:flow time/(h: s)	3.76	3.60	3.52
Improve on QMOM		4.2%	6.4%
Improve on DQMOM			2.2%

problem of the negative abscissas is avoided. In the meanwhile, a special algorithm for solving the Vandermonde linear system makes the algorithm efficient and accurate. In theory, this algorithm can track arbitrary number of moments, which is one of our main tasks in the next step. In conclusion, application of FPQMOM for solving PBE in CFD-PBM coupled model is reasonable and with it more reliable results can be obtained relative to QMOM and DQMOM Therefore, we recommend the FPQMOM for solving the PBEs in CFD-PBM coupled framework for considering the effect of the polydispersity on the system dynamic behaviors. Further researches on the improvement of the CFD-PBM coupled model in FBR are in progress in our group.

Notation

B_{ag} birth rate of particles due to aggregation (s^{-1})
B_{br} birth rate of particles due to breakage (s^{-1})
C_{μ}, $C_{1\varepsilon}$, $C_{2\varepsilon}$ coefficients in turbulence model
C_D drag coefficient
$C_{p,g}$ heat capacity coefficient of gas phase ($kJ \cdot kg^{-1} \cdot K^{-1}$)
$C_{p,s}$ heat capacity coefficient of solid phase ($kJ \cdot kg^{-1} \cdot K^{-1}$)
$[C^*]$ active catalyst site concentration ($kmol \cdot kg_{cat}^{-1}$)
d_s particle diameter (m)
d_{32} Sauter Diameter (m)
D_{ag} death rate of particles due to aggregation (s^{-1})
D_{ag} death rate of particles due to breakage (s^{-1})
e_s particle–particle restitution coefficient
g gravitational constant ($m \cdot s^{-2}$)
G particle growth rate ($m \cdot s^{-1}$)
h_g specific enthalpy of the gas ($kJ \cdot kg^{-1} \cdot K^{-1}$)
h_s specific enthalpy of the solid ($kJ \cdot kg^{-1} \cdot K^{-1}$)
h_i specific enthalpy of the ith phase ($kJ \cdot kg^{-1} \cdot K^{-1}$)
$\bar{\bar{I}}$ identity matrix
k specified number of moments
k_s shape factor (π)
k_v shape factor ($\pi/6$)
K an aggregation rate constant ($m^{-6} \cdot s^{-1}$)
L_0 initial particle diameter (m)
L, L_i, L_j particle diameter (m)
m_k the kth moment of number density function (m^k)
[M] monomer concentration ($mol \cdot m^{-3}$)
$m^{\bullet}_{sp}$ mass transfer rate between the gas and solid phase
Nu_s Nusselt number of solid phase (dimensionless)
N the number of quadrature nodes
p_s particulate phase pressure (Pa)
ΔP_s pressure drop described by the buoyant weight of the suspension ($K \cdot Pa$)
ΔP_g the effect of gas phase weight on the pressure weight ($K \cdot Pa$)
Pr Prandtl number of liquid phase (dimensionless)
q_i heat flux ($W \cdot m^{-2}$)
Q_{gs} intensity of heat exchange between gas and solid phases ($W \cdot s^{-1} \cdot m^{-3}$)
Re_s Reynolds number
t flow time (s)
T_g gas temperature (K)
T_s solid temperature (K)
T_{sf} the average polymer melting temperature of size L_i and L_j (K)
$\vec{u}$ particle growth rate vector due to processes other than interaction with other particles ($m \cdot s^{-1}$)
$\vec{v}_g$ gas velocity ($m \cdot s^{-1}$)
$\vec{v}_s$ particle velocity ($m \cdot s^{-1}$)
V_i characteristic volume (m^3)
w_i quadrature weight (dimensionless)

Greek symbols

α_g volume fraction of gas phase
α_s volume fraction of solid phase
β inter-phase momentum transfer coefficient ($kg \cdot m^{-3} \cdot s^{-1}$)
ε turbulence dissipation rate ($m^2 \cdot s^{-3}$)
μ_g viscosity of gas phase ($Pa \cdot s$)
μ_s solid shear viscosity ($Pa \cdot s$)
$\mu_{s,col}$ solid collisional viscosity ($Pa \cdot s$)
$\mu_{s,kin}$ solid kinetic viscosity ($Pa \cdot s$)
$\mu_{s,fr}$ solid frictional viscosity ($Pa \cdot s$)
σ_{ε} granular kinetic theory parameter (kinetic viscosity) ($Pa \cdot s$)
θ angle of internal friction (°)
Θ_s granular temperature ($m^2 \cdot s^{-2}$)
γ_{Θ_s} the collisional dissipation of energy ($m^2 \cdot s^{-2}$)
$\bar{\bar{\tau}}_g$ shear stress of gas phase ($N \cdot m^{-2}$)
$\bar{\bar{\tau}}_s$ shear stress of solid phase ($N \cdot m^{-2}$)
ρ_g density of gas mixture ($kg \cdot m^{-3}$)
ρ_s density of solid ($kg \cdot m^{-3}$)
λ_s solid bulk viscosity ($Pa \cdot s$)
κ_i thermal conductivity for phase i ($W \cdot m^{-1} \cdot K^{-1}$)
κ_{gs} thermal conductivity of liquid phase of interphase ($W \cdot m^{-1} \cdot K^{-1}$)
ω the correction factor in EMMS drag model
ζ_i weight abscissas (m)
$\Delta Q_{rs\alpha}$ heat produced from polymerization reaction ($kJ \cdot kmol^{-1}$)

Subscripts

g gas phase
s solid phase

Acknowledgments

The authors thank the National Natural Science Foundation of China (No. 201076171), the National Ministry of Science and Technology of China (No. 2012CB21500402) and the Research Fund for the Doctoral Program of Higher Education (No. 20130073110077) for supporting this work.

References

[1] D.P. Shi, Z.H. Luo, A.Y. Guo, Numerical simulation of the gas–solid flow in fluidized-bed polymerization reactors, Ind. Eng. Chem. Res. 49 (2010) 4070–4079.
[2] J. Werther, E.U. Hartge, A population balance model of the particle inventory in a fluidized-bed reactor/regenerator system, Powder Technol. 148 (2004) 113–122.
[3] A. Puettmann, E.U. Hartge, J. Werther, Application of the flowsheet simulation concept to fluidized bed reactor modeling. Part I: Development of a fluidized bed reactor simulation module, Chem. Eng. Process. 60 (2012) 86–95.
[4] O. Ashrafi, N. Mostoufi, R. Sotudeh-Gharebage, Two phase steady-state particle size distribution in a gas-phase fluidized bed ethylene polymerization reactor, Chem. Eng. Sci. 73 (2012) 1–7.
[5] Z.H. Luo, S.H. Wen, D.P. Shi, Z.W. Zheng, Coupled single particle and population balance modeling for particle size distribution of polypropylene produced in loop reactors, Macromol. React. Eng. 4 (2010) 123–134.
[6] R. Fan, Computational fluid dynamics simulation of fluidized bed polymerization reactors(PHD thesis) Iowa State University, Iowa, USA, 2006.
[7] I. Petrovsky, Lectures on the Theory of Integral Equations, Graylock Press, USA, 1957.
[8] S. Kumar, D. Ramkrishna, On the solution of population balance equations by discretization—I. A fixed pivot technique, Chem. Eng. Sci. 51 (1996) 1311–1332.
[9] A. Krallis, D. Meimaroglou, C. Kiparissides, Dynamic prediction of the bivariate molecular weight–copolymer composition distribution using sectional-grid and stochastical numerical methods, Chem. Eng. Sci. 63 (2008) 4342–4360.
[10] H.M. Hulburt, S. Katz, Some problems in particle technology: a statistical mechanical formulation, Chem. Eng. Sci. 19 (1964) 555–574.
[11] J.L. Favero, F.L.R. Silva, P.L.C. Lage, Comparision of methods for multivariate moment inversion—introducing the independent component analysis, Comput. Chem. Eng. 60 (2014) 41–56.

[12] R. McGraw, Description of the aerosol dynamics by the quadrature method of moments, Aerosol Sci. Technol. 27 (1997) 255–265.
[13] D.L. Marchisio, R.D. Vigil, R.O. Fox, Quadrature method of moments for aggregation breakage processes, J. Colloid Interface Sci. 258 (2003) 322–334.
[14] D.L. Marchisio, J.T. Pikturna, R.O. Fox, R.D. Vigil, Quadrature method of moments for population balance equations, AIChE J. 49 (2003) 1266–1276.
[15] D.L. Marchisio, R.D. Vigil, R.O. Fox, Implementation of the quadrature method of moments in CFD codes for aggregation-breakage problems, Chem. Eng. Sci. 58 (2003) 3337–3351.
[16] J.L. Favero, P.L.C. Lage, The dual-quadrature method of generalized moments using automatic integration packages, Comput. Chem. Eng. 38 (2012) 1–10.
[17] J.C. Cheng, R.O. Fox, Kinetic modeling of nanoprecipitation using CFD coupled with a population balance, Ind. Eng. Chem. Res. 49 (2010) 10651–10662.
[18] E. Aamir, Z.K. Nagy, C.D. Rielly, T. Kleinert, B. Judat, Combined quadrature method of moments and method of characteristics approach for efficient solution of population balance models for dynamic modeling and crystal size distribution control of crystallization processes, Ind. Eng. Chem. Res. 48 (2009) 8575–8586.
[19] D.L. Marchisio, R.O. Fox, Solution of population balance equations using the direct quadrature method of moments, J. Aerosol Sci. 36 (2005) 43–73.
[20] R.O. Fox, Bivariate direct quadrature method of moments for coagulation and sintering of particle populations, J. Aerosol Sci. 37 (2006) 1562–1580.
[21] R. Fan, D.L. Marchisio, R.O. Fox, Application of the direct quadrature method of moments to polydisperse gas–solid fluidized beds, Powder Technol. 139 (2004) 7–18.
[22] M.M. Attarakih, C. Drumm, H.J. Bart, Solution of the population balance equation using the sectional quadrature method of moments (SQMOM), Chem. Eng. Sci. 64 (2009) 742–752.
[23] C.A. Dorao, H.A. Jakobsen, Numerical calculation of the moments of the population balance equation, J. Comput. Appl. Math. 196 (2006) 619–633.
[24] R. Grosch, H. Briesen, W. Marquardt, M. Wukkow, Generalization and numerical investigation of QMOM, AIChE J. 53 (2006) 207–277.
[25] A. Buffo, M. Vanni, D.L. Marchisio, R.O. Fox, Multivariate quadrature-based moments methods for turbulent polydisperse gas–liquid systems, Int. J. Multiphase Syst. 50 (2013) 41–57.
[26] J. Sanyal, D.L. Marchisio, R.O. Fox, K. Dhanasekharan, On the comparison between population balance models for CFD simulation of bubble columns, Ind. Eng. Chem. Res. 44 (2005) 5063–5072.
[27] R.O. Fox, Introduction and fundamentals of modeling approaches for polydisperse multiphase flow, CISM Course on Multiphase Reacting Flows-Modelling and Simulation: Udine, Italy, 2006, pp. 1–40.
[28] C. Yuan, F. Laurent, R.O. Fox, An extended quadrature method of moments for population balance equations, J. Aerosol Sci. 51 (2012) 1–23.
[29] Z.L. Gu, J.W. Su, J.Y. Jiao, X.Y. Xu, Simulation of micro-behaviors including nucleation, growth, aggregation in particle system, Sci. China Ser. B Chem. 52 (2009) 241–248.
[30] J.W. Su, Z.L. Gu, X.Y. Xu, Advances in numerical methods for the solution of population balance equations for disperse phase systems, Sci. China Ser. B Chem. 52 (2009) 1063–1079.
[31] J.W. Su, Z.L. Gu, Y. Li, S.Y. Feng, X.Y. Xu, Solution of population balance equation using quadrature method of moments with an adjustable factor, Chem. Eng. Sci. 62 (2007) 5897–5911.
[32] Z.L. Gu, J.W. Su, Y. Li, S.Y. Feng, Behaviors of the dispersed phase in the multiphase system and population balance model (in Chinese), Chem. React. Eng. Technol. 23 (2007) 162–167.
[33] A. Ahmadzadeh, H. Arastoopour, F. Teymour, M. Strumendo, Population balance equations' application in rotating fluidized bed polymerization reactor, Chem. Eng. Res. Des. 86 (2008) 329–343.
[34] L. Mazzei, D.L. Marchisio, P. Lettieri, New quadrature-based moment method for the mixing of inert polydisperse fluidized powders in commercial CFD codes, AIChE J. 58 (2012) 3054–3069.
[35] X.Z. Chen, Z.H. Luo, W.C. Yan, Y.H. Lu, I.S. Ng, Three-dimensional CFD-PBM coupled model of the temperature fields in fluidized bed polymerization reactors, AIChE J. 57 (2011) 3351–3366.
[36] W.C. Yan, Z.H. Luo, Y.H. Lu, X.D. Chen, A CFD-PBM-PMLM integrated model for the gas–solid flow fields in fluidized bed polymerization reactors, AIChE J. 58 (2012) 1717–1732.
[37] W.C. Yan, J. Li, Z.H. Luo, A CFD-PBM coupled model with polymerization kinetics for multizone circulating polymerization reactors, Powder Technol. 231 (2012) 77–87.
[38] J. Li, Z.H. Luo, X.Y. Lan, C.M. Xu, J.S. Gao, Numerical simulation of the turbulent gas–solid flow and reaction in a polydisperse FCC riser reactor, Powder Technol. 237 (2013) 569–580.
[39] R. Fan, R.O. Fox, Segregation in polydisperse fluidized beds: validation of a multi-fluid model, Chem. Eng. Sci. 63 (2008) 272–285.
[40] L. Mazzei, D.L. Marchisio, P. Lettieri, Direct quadrature method of moments for the mixing of inert polydisperse fluidized powders and the role of numerical diffusion, Ind. Eng. Chem. Res. 49 (2010) 5141–5155.
[41] A. Dutta, D. Constales, G.J. Heynderickx, Applying the direct quadrature method of moments to improve multiphase FCC riser reactor simulation, Chem. Eng. Sci. 83 (2012) 93–109.
[42] L. Mazzei, Limitations of quadrature-based moment methods for modeling inhomogeneous polydisperse fluidized powders, Chem. Eng. Sci. 66 (2011) 3628–3640.
[43] A. Buffo, M. Vanni, D.L. Marchisio, Modeling and simulation of turbulent polydisperse gas–liquid systems via the generalized population balance equation, Rev. Chem. Eng. 30 (2014) 73–126.
[44] X.Z. Chen, D.P. Shi, X. Gao, Z.H. Luo, A fundamental CFD study of the gas–solid flow field in fluidized bed polymerization reactors, Powder Technol. 205 (2011) 276–288.
[45] D.J. Gunn, Transfer of heat or mass to particles in fixed and fluidized beds, Int. J. Heat Mass Transfer 21 (1987) 467–475.
[46] N. Yang, W. Wang, W. Ge, J. Li, CFD simulation of concurrent-up gas–solid flow in circulating fluidized bed with structure—dependent drag coefficient, Chem. Eng. J. 96 (2003) 71–80.
[47] N. Yang, W. Wang, W. Ge, L. Wang, J. Li, Simulation of heterogeneous structure in a circulating fluidized-bed riser by combining the two-fluid model with the EMMS approach, Ind. Eng. Chem. Res. 43 (2004) 5548–5561.
[48] R.G. Gordon, Error bounds in equilibrium statistical mechanics, J. Math. Phys. 9 (1968) 655–663.
[49] G.H. Golub, C.F. Vanloan, Matrix Computations, 3rd ed. The Johns Hopkins Univ Press, Baltimore, 1996. 183–188.
[50] J.J. Zacca, W.H. Ray, Modeling of the liquid phase polymerization of olefins in loop reactors, Chem. Eng. Sci. 48 (1993) 3743–3765.
[51] H. Arastoopour, C.S. Huang, S.A. Weil, Fluidization behavior of particles under agglomerating conditions, Chem. Eng. Sci. 43 (1988) 3063–3075.
[52] H. Yiannouslakis, A. Yiagopoulos, C. Kiparissides, Recent developments in the particle size distribution modeling of fluidized bed olefin polymerization reactors, Chem. Eng. Sci. 56 (2001) 917–925.
[53] S. Patankar, Numerical Heat Transfer and Fluid Flow, Hemisphere Publishing Corporation, 1980.
[54] W. Barth, Flow patterns during the conveyance of solid particles and droplets in gases, Chem. Ing. Tech. 30 (1958) 171–180.
[55] C. Loha, H. Chattopadhyay, P.K. Chatterjee, Assessment of drag models in simulating bubbling fluidized bed hydrodynamics, Chem. Eng. Sci. 75 (2012) 400–407.
[56] C.K.K. Lun, S.B. Savage, D.J. Jeffrey, N. Chepurniy, Kinetic theories for granular flow-inelastic particles in couette-flow and slightly inelastic particles in a general flow field, J. Fluid Mech. 140 (1984) 223–232.
[57] J. Ding, D. Gidaspow, A bubbling fluidization model using kinetic-theory of granular flow, AIChE J. 36 (1990) 523–538.
[58] M. Syamlal, W. Rogers, T.J. O'Brien, MFIX Documentation, Theory Guide, vol. 1, National Technology Information Service, Springfield, 1993.
[59] D. Gidaspow, Multiphase Flow and Fluidization: Continuum and Kinetic Theory Descriptions, Academic Press, Boston, 1994.
[60] D.G. Schaeffer, Instability in the evolution equations describing incompressible granular flow, J. Differ. Equ. 66 (1987) 19–50.
[61] P. Bradshaw, T. Cebeci, J.H. Whitelaw, Engineering Calculation Methods for Turbulent Flow, Academic Press, London, 1981.
[62] C.J. Chen, S.Y. Jaw, Fundamentals of Turbulence Modeling, Taylor & Francis, Washington, 1998.
[63] K. Atsonios, A. Nikolopoulos, S. Karellas, N. Nikolopoulos, P. Grammelis, Em. Kakaras, Numerical investigation of the grid spatial resolution and the anisotropic character of EMMS in CFB multiphase flow, Chem. Eng. Sci. 66 (2011) 3979–3990.
[64] A. Nikolopoulos, N. Nikolopoulos, N. Varveris, S. Karellas, P. Grammelis, Em. Kakaras, Investigation of porper modeling of very dense granular flows in the recirculation system of CFBs, Particuology 10 (2012) 699–709.